ATLAS CONF Note

ATLAS-CONF-2018-042

26th July 2018

Search for direct chargino pair production with W-boson mediated decays in events with two leptons and missing transverse momentum at $\sqrt{s} = 13$ TeV with the ATLAS detector

The ATLAS Collaboration

The results of a search for the direct pair production of charginos decaying via W-bosons are reported using 80.5 fb^{-1} of integrated luminosity from LHC pp collisions at 13 TeV collected by the ATLAS detector in the 2015, 2016 and 2017 data taking campaigns. Charginos are searched for in final states with two isolated leptons (electron or muon), missing transverse momentum and at most one light jet in the final state. No excess above Standard Model expectations is observed. Exclusion limits are derived on the chargino mass assuming a simplified model in which it decays with a 100% branching ratio to an on-shell W-boson and the lightest neutralino: $\tilde{\chi}_1^{\pm} \rightarrow W^{\pm}\tilde{\chi}_1^0$. For a massless neutralino, chargino masses up to 410 GeV are excluded at 95% confidence level.

ATLAS-CONF-2018-042
27 July 2018

1 Introduction

Weak scale Supersymmetry (SUSY) [1–6] is a theoretical extension to the Standard Model (SM) which, if realised in nature, would solve the hierarchy problem [7–10] through the addition of a new fermion/boson supersymmetric partner to each boson/fermion in the SM. In SUSY models which conserve R-parity [11], SUSY particles (sparticles) must be produced in pairs and the lightest supersymmetric particle (LSP) is stable and can be weakly interacting, thus often constituting a viable candidate for dark matter [12, 13]. Due to its stability, any LSP produced at the Large Hadron Collider (LHC) would escape detection and give rise to missing transverse momentum ($\mathbf{p}_{\mathrm{T}}^{\mathrm{miss}}$) in the final state, which can be used to discriminate SUSY signals from the SM background.

LHC sparticle production cross-sections are highly dependent on the sparticle masses. The coloured sparticles (squarks and gluinos) are strongly produced and have significantly larger production cross-sections than non-coloured sparticles of equal masses, such as the sleptons (superpartners of the SM leptons) and the electroweakinos. The superpartners of the SM Higgs and the electroweak gauge bosons, known as higgsinos, winos and bino are collectively known as electroweakinos. They mix to form chargino ($\tilde{\chi}_i^{\pm}, i = 1, 2$) and neutralino ($\tilde{\chi}_j^0, j = 1, 2, 3, 4$) mass eigenstates (states are ordered by increasing values of their mass). If gluino and squark masses were much heavier than low-mass electroweakinos, then SUSY production at the LHC would be dominated by direct electroweak production. The latest ATLAS limits on squark and gluino production [14] extend well beyond the TeV scale, thus making electroweak production of sparticles a promising and important probe to search for SUSY at the LHC.

This analysis targets the direct production of $\tilde{\chi}_1^+\tilde{\chi}_1^-$, where each chargino decays to the $\tilde{\chi}_1^0$ (considered as the LSP) and a real W-boson. Only the leptonic decay mode of the W-boson is considered, so the events are characterised by the presence of two isolated leptons (e, μ) with opposite charge, and significant $\mathbf{p}_{\mathrm{T}}^{\mathrm{miss}}$ (whose magnitude is referred to as $E_{\mathrm{T}}^{\mathrm{miss}}$), expected from neutrinos and LSPs in the final states. A simplified model [15] is considered for the signal, assuming a branching ratio of 100% for the decay under study. In the simplified models the masses of the relevant sparticles, in this case $\tilde{\chi}_1^{\pm}$ and $\tilde{\chi}_1^0$, are the only free parameters. The cross-section for chargino pair production is assumed to be that corresponding to a wino-like state.

A diagram of the process considered is shown in Figure 1.

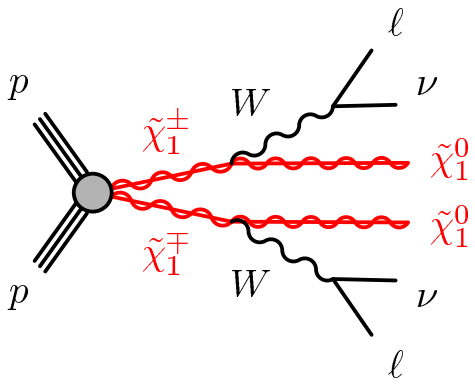

Figure 1: Diagram of the supersymmetric model considered in this note.

Due to significant background contributions from SM WW production and the low expected signal cross-section (58.6 ± 4.7 fb for a chargino mass of 400 GeV), the analysis of this channel is challenging.

This analysis uses the 2015, 2016 and 2017 ATLAS datasets to target intermediate chargino masses in areas of the parameter space previously not excluded by the corresponding ATLAS Run-1 search [16] and by a recent CMS search at 13 TeV [17] in the same channel. After a brief description of the ATLAS detector in Section 2, the data and simulated Monte Carlo (MC) samples used in the analysis are detailed in Section 3. Section 4 and Section 5 present the event reconstruction and the search strategy. The SM background estimation and the systematic uncertainties are discussed in Section 6 and Section 7, respectively. Finally, results and their interpretation are reported in Section 8. Section 9 summarizes the conclusions.

2 ATLAS detector

The ATLAS detector [18] at the LHC is a general purpose detector with a forward-backward symmetric cylindrical geometry and an almost complete coverage in solid angle around the collision point.[1] It consists of an inner tracking detector surrounded by a thin superconducting solenoid, electromagnetic and hadronic calorimeters, and a muon spectrometer incorporating three large superconducting toroid magnets. The inner-detector system (ID) is immersed in a 2 T solenoidal axial magnetic field and provides charged particle tracking in the range $|\eta| < 2.5$. It consists of a high-granularity silicon pixel detector, a silicon microstrip tracker and a transition radiation tracker, which enables radially extended track reconstruction up to $|\eta| = 2.0$. The transition radiation tracker also provides electron identification information. During the first LHC long shutdown, a new tracking layer, known as the Insertable B-Layer (IBL) [19], was added with an average sensor radius of 33 mm from the beam pipe in order to improve tracking and b-tagging performance. The calorimeter system covers the pseudorapidity range $|\eta| < 4.9$. Within the region $|\eta| < 3.2$, electromagnetic calorimetry is provided by barrel and endcap high-granularity lead/liquid-argon (LAr) electromagnetic sampling calorimeters. Hadronic calorimetry is provided by a steel/scintillating-tile sampling calorimeter within $|\eta| < 1.7$, and two copper/LAr hadronic endcap calorimeters. The solid angle coverage is completed with forward copper/LAr and tungsten/LAr calorimeter modules optimised for electromagnetic and hadronic measurements respectively. The muon spectrometer (MS) comprises separate trigger and high-precision tracking chambers measuring the deflection of muons in a magnetic field generated by superconducting air-core toroids. The precision chamber system covers the region $|\eta| < 2.7$ with three layers of monitored drift tubes, complemented by cathode strip chambers in the forward region, where the background is higher. The muon trigger system covers the range $|\eta| < 2.4$ with resistive plate chambers in the barrel, and thin gap chambers in the endcap regions.

A two-level trigger system is used to select events. There is a low-level hardware trigger implemented in custom electronics, which reduces the incoming data rate to a design value of 100 kHz using a subset of detector information, and a high-level software trigger which selects interesting final state events with algorithms accessing the full detector information, and further reduces the rate to ~1 kHz [20] .

[1] ATLAS uses a right-handed coordinate system with its origin at the nominal interaction point (IP) in the centre of the detector and the z-axis along the beam pipe. The x-axis points from the IP to the centre of the LHC ring, and the y-axis points upwards. Cylindrical coordinates (r, ϕ) are used in the transverse plane, ϕ being the azimuthal angle around the z-axis. The pseudorapidity is defined in terms of the polar angle θ as $\eta = -\ln\tan(\theta/2)$. Rapidity is defined as $y = 0.5\ln[(E+p_z)/(E-p_z)]$, where E and p_z denote the energy and the component of the particle momentum along the beam direction, respectively. Angular distance is measured in units of $\Delta R \equiv \sqrt{(\Delta\eta)^2 + (\Delta\phi)^2}$.

3 Data and simulated event samples

The data used in this analysis were collected by the ATLAS detector in 2015, 2016 and 2017 during pp collisions at a center-of-mass energy of $\sqrt{s}$ = 13 TeV, with an average number of additional pp interactions per bunch crossing (pile-up) of $\langle\mu\rangle$ = 14 in 2015, $\langle\mu\rangle$ = 25 in 2016 and $\langle\mu\rangle$ = 38 in 2017. After data-quality requirements, the data sample amounts to an integrated luminosity of 36.2 fb^{-1} collected in 2015-2016, and 44.3 fb^{-1} in 2017. The uncertainty on the integrated luminosity of the combined 2015-2017 dataset amounts to 2%. It is derived, following a methodology similar to that detailed in Ref. [21], from calibrations of the luminosity scale using x-y beam-separation scans performed in August 2015, May 2016 and July 2017. The results for 2017 are still preliminary.

Events considered in this analysis must pass a trigger selection requiring at least two electrons or two muons or an electron-muon pair. The trigger-level thresholds on the p_{T} value of the leptons involved in the trigger decision are different according to the data taking periods. They are in the range 8-22 GeV for data collected in 2015 and 2016, and 8-24 GeV for data collected in 2017. These thresholds are looser than those applied in the lepton offline selection to ensure that trigger efficiencies are constant in the relevant phase space.

MC simulated event samples are used for the SM background estimate and to model the SUSY signal. The MC samples are processed through an ATLAS detector simulation [22] based on Geant4 [23] or a fast simulation using a parametrisation of the ATLAS calorimeter response and Geant4 for the other components of the detector. They are reconstructed with the same algorithms as used for the data. To compensate for differences between data and MC simulation in the lepton reconstruction efficiency, energy scale and energy resolution, in the b-tagging efficiency and in the modelling of the trigger, correction factors are derived from data and applied to the samples of simulated events.

The event generation configurations of all SM backgrounds used are listed in Table 1 with the relevant parton distribution function (PDF) set, the configuration of underlying-event and hadronisation parameters (underlying-event tune) and the cross-section calculation order in α_S used to normalise the event yields for these samples.

The SUSY signal samples are generated from leading-order (LO) matrix elements with up to two extra partons using MadGraph5_aMC@NLO v2.6.1 [24] interfaced to Pythia version 8.186 [25], with the A14 tune [26], for the modelling of the SUSY decay chain, parton showering, hadronisation and the description of the underlying event. Parton luminosities are provided by the NNPDF23LO PDF set [27]. Jet-parton matching has been performed following the CKKW-L prescription [28], with a matching scale set to one quarter of the mass of the pair-produced $\tilde{\chi}_1^{\pm}$. Signal cross-sections are calculated at NLO, with soft gluon emission effects added at next-to-leading-logarithm (NLL) accuracy [29–33]. The nominal cross-section and its uncertainty are taken from an envelope of cross-section predictions using different PDF sets and factorization and renormalization scales, as described in Ref. [34].

Minimum-bias interactions were generated and overlaid on top of the hard-scattering process to simulate the effect of multiple pp interactions occurring during the same (in-time) or a nearby (out-of-time) bunch-crossing. These were produced using Pythia version 8.186 with the A2 tune [35] and the MSTW2008LO PDF [36] set. The MC samples are reweighted so that the distribution of the average number of interactions per bunch-crossing matches the observed distribution in the data.

Table 1: Simulated background event samples used in this analysis with the corresponding matrix element and parton shower generators, cross-section order in α_S used to normalise the event yield, underlying-event tune and PDF set.

Physics process	Generator	Parton shower	Cross-section	Tune	PDF set
$t\bar{t}$	Powheg Box v2[37, 38] r3026	Pythia 8.186[25]	NNLO+NNLL	Perugia2012[39]	NL0 CT10[40]
$t\bar{t}+V(V=W,Z)$	MG5_aMC@NLO[24]	Pythia 8.186	NLO	A14[26]	NNPDF2.3LO[27]
$t\bar{t}+WW$	MG5_aMC@NLO	Pythia 8.186	LO	A14	NNPDF2.3LO
$tZ, t\bar{t}t\bar{t}, t\bar{t}t$	MG5_aMC@NLO	Pythia 8.186	NLO	A14	NNPDF2.3LO
single top	Powheg Box v2 r2856	Pythia 6.428[41]	Approx. NNLO	Perugia2012	NLO CT10
$Z/\gamma^*(\rightarrow ll)+jets$	Sherpa 2.2.1[42]	Sherpa 2.2.1	NNLO	Sherpa default	NNPDF3.0nnlo[43]
WW, WZ, ZZ	Powheg Box v2	Pythia 8.210	NLO	AZNLO[44]	CTEQ6L1[45]
$VVV(V=W,Z)$	Sherpa 2.2.2	Sherpa 2.2.2	NLO	Sherpa default	NNPDF3.0nnlo
Higgs	Pythia 8.186	Pythia 8.186	NLO	A14	NNPDF2.3LO

4 Object identification

Leptons selected for analysis are categorised as baseline or signal leptons according to various quality and kinematic selection criteria. Baseline objects are used in the calculation of missing transverse momentum, to resolve ambiguity between the analysis objects in the event and in the fake/non-prompt lepton (FNP) background estimation described in Section 6. Leptons used for the final event selection must pass more stringent signal requirements.

Baseline electron candidates are reconstructed using energy clusters in the electromagnetic calorimeter which are matched to an ID track. They are required to pass a *loose* likelihood-based identification requirement [46], to have a transverse momentum $p_{\mathrm{T}} > 10$ GeV and to reside within the pseudorapidity region $|\eta| < 2.47$. They are also required to be within $|z_0 \sin\theta| = 0.5$ mm of the primary vertex[2], where z_0 is the longitudinal impact parameter with respect to the primary vertex. Signal electrons are required to satisfy a *medium* identification requirement [46] and to be isolated from other objects in the event according to a p_{T}-dependent isolation requirement. This requirement uses calorimeter and track-based information to obtain 95% efficiency at $p_{\mathrm{T}} = 25$ GeV for $Z \rightarrow ee$ events, rising to 99% efficiency at $p_{\mathrm{T}} = 60$ GeV. Finally, the track associated with the signal electron must have a significance of the transverse impact parameter with respect to the reconstructed primary vertex, d_0, of $|d_0|/\sigma(d_0) < 5$.

Baseline muon candidates are reconstructed in the pseudorapidity region $|\eta| < 2.7$ from muon spectrometer tracks matching ID tracks. They are required to have $p_{\mathrm{T}} > 10$ GeV, to be within $|z_0 \sin\theta| = 0.5$ mm of the primary vertex and to satisfy the *medium* identification requirements defined in Ref. [47]. The *medium* identification criterion defines requirements on the number of hits in the different ID and muon spectrometer subsystems, and on the significance of the charge to momentum ratio q/p. Signal muons are required to be isolated: calorimeter and track-based isolation criteria are used to obtain 95% efficiency at $p_{\mathrm{T}} = 25$ GeV for $Z \rightarrow \mu\mu$ events, rising to 99% efficiency at $p_{\mathrm{T}} = 50$ GeV. Finally, the track associated with the signal muon must have a significance of the transverse impact parameter with respect to the reconstructed primary vertex, d_0, of $|d_0|/\sigma(d_0) < 3$.

Jets are reconstructed from topological energy clusters in the calorimeter [48] using the anti-k_t jet clustering algorithm [49] with a radius parameter $R = 0.4$. The reconstructed jets are then calibrated by the application of a jet energy scale (JES) derived from 13 TeV data and simulation [50]. Only jet

[2] The primary vertex is defined as the vertex with at least two associated tracks and with the highest scalar sum of the squared transverse momentum of the associated tracks.

candidates with $p_{\mathrm{T}} > 20\,\mathrm{GeV}$ and $|\eta| < 2.4$ are considered as selected jets in the analysis, although jets with $|\eta| < 4.9$ are included in the missing transverse momentum estimate.

In order to reduce the effects of pile-up, for jets with $p_{\mathrm{T}} < 60\,\mathrm{GeV}$ and $|\eta| < 2.4$ a significant fraction of the tracks associated with each jet must have an origin compatible with the primary vertex, as defined by the jet vertex tagger [51]. This requirement reduces jets from pile-up to 1‰, with an efficiency for pure hard scatter jets of 92%. Finally, events containing a jet that does not pass jet quality requirements [52, 53] are vetoed in order to remove events impacted by detector noise and non-collision backgrounds.

The MV2C10 boosted decision tree algorithm [54] identifies jets containing b-hadrons ("b-tagged jets" or "b-jets") by using quantities such as the impact parameters of associated tracks and positions of any good reconstructed secondary vertices. A selection that provides 85% efficiency for tagging b-jets in simulated $t\bar{t}$ events is used. The corresponding rejection factors against jets originating from c-quarks, from τ-leptons, and from light quarks and gluons in the same sample at this working point are 2, 6 and 27, respectively.

To avoid the double counting of analysis baseline objects, an overlap removal procedure is applied in the following steps:

- jet candidates within $\Delta R = \sqrt{\Delta y^2 + \Delta\phi^2} < 0.2$ (where y stands for the rapidity) of an electron candidate are removed;
- jets with fewer than three tracks which lie within $\Delta R < 0.4$ around a muon candidate are removed;
- electrons and muons within $\Delta R < 0.4$ to the remaining jets are discarded, in order to reject leptons from the decay of a b- or c-hadron;
- electron candidates are rejected if they are found to share an inner detector track with a muon.

The missing transverse momentum is defined as the negative vector sum of the transverse momenta of all identified baseline physics objects. Low momentum contributions from particle tracks from the primary vertex which are not associated with reconstructed analysis objects are included in the calculation. Associated to the $E_{\mathrm{T}}^{\mathrm{miss}}$ value is the $E_{\mathrm{T}}^{\mathrm{miss}}$ significance value, obtained taking into account the total expected longitudinal (parallel to $\mathbf{p}_{\mathrm{T}}^{\mathrm{miss}}$) momentum resolution of all jets and leptons at a given p_{T} added in the $E_{\mathrm{T}}^{\mathrm{miss}}$ calculation, and a correlation factor between each jet's or lepton's longitudinal and transverse momentum resolution (again with respect to the $\mathbf{p}_{\mathrm{T}}^{\mathrm{miss}}$), as further detailed in Ref. [55]. The $E_{\mathrm{T}}^{\mathrm{miss}}$ significance helps to discriminate events where the vector sum of the particle-level transverse momenta of invisible particles in the event is different from zero (e.g. arising from events with true $E_{\mathrm{T}}^{\mathrm{miss}}$) and events where it is zero (e.g. arising from poorly measured particles/jets).

5 Search strategy

Events used in this search are required to have exactly two opposite-sign signal leptons, which must satisfy $p_{\mathrm{T}} > 25$ GeV. In order to remove contributions from low mass resonances, the invariant mass of the two leptons must be $m_{\ell\ell} > 25$ GeV. Events are further required to have no reconstructed b-jets, to suppress contributions of processes with top quarks. Selected events must have in addition $E_{\mathrm{T}}^{\mathrm{miss}} > 110$ GeV and $E_{\mathrm{T}}^{\mathrm{miss}}$ significance > 10.

The stransverse mass m_{T2} [56, 57] is a kinematic variable used to bound the masses of a pair of particles that are presumed to have each decayed semi-invisibly into one visible and one invisible particle. It is defined as

$$m_{\mathrm{T2}}(\mathbf{p}_{\mathrm{T},1}, \mathbf{p}_{\mathrm{T},2}, \mathbf{q}_{\mathrm{T}}) = \min_{\mathbf{q}_{\mathrm{T},1}+\mathbf{q}_{\mathrm{T},2}=\mathbf{q}_{\mathrm{T}}} \left\{ \max[\, m_{\mathrm{T}}(\mathbf{p}_{\mathrm{T},1}, \mathbf{q}_{\mathrm{T},1}), m_{\mathrm{T}}(\mathbf{p}_{\mathrm{T},2}, \mathbf{q}_{\mathrm{T},2}) \,] \right\}, \tag{1}$$

where m_{T} indicates the transverse mass[3], $\mathbf{p}_{\mathrm{T},1}$ and $\mathbf{p}_{\mathrm{T},2}$ are the transverse momentum vectors of the two leptons, and $\mathbf{q}_{\mathrm{T},1}$ and $\mathbf{q}_{\mathrm{T},2}$ are vectors with $E_{\mathrm{T}}^{\mathrm{miss}} = \mathbf{q}_{\mathrm{T},1} + \mathbf{q}_{\mathrm{T},2}$. The minimisation is performed over all the possible decompositions of $\mathbf{q}_{\mathrm{T}}$. For $t\bar{t}$ or WW decays, assuming an ideal detector with perfect momentum resolution, $m_{\mathrm{T2}}(\ell, \ell, E_{\mathrm{T}}^{\mathrm{miss}})$ has a kinematic endpoint at the mass of the W-boson. Signal models with sufficient mass splittings between the $\tilde{\chi}_1^{\pm}$ and the $\tilde{\chi}_1^0$ feature m_{T2} distributions that extend beyond this kinematic endpoint expected for the dominant SM backgrounds. Therefore, events in this search are required to have high m_{T2} values.

Events are separated into "same flavour" (SF) events, i.e. dielectron e^+e^- and di-muon $\mu^+\mu^-$, and "different flavour" (DF) events, i.e. $e^{\pm}\mu^{\mp}$, with the split being motivated by different background compositions in the two classes of events. SF events are required to have a di-lepton invariant mass outside the Z-mass window ($|m_{\ell\ell} - m_Z| > 30$ GeV).

Events are further classified by the multiplicity of non-b-tagged jets ($n_{\text{non-}b\text{-tagged jets}}$), i.e. the number of jets not identified as b-jets by the MV2C10 boosted decision tree algorithm. All events are required to have $n_{\text{non-}b\text{-tagged jets}} \leq 1$. Following the classification of the events, two sets of signal regions (SRs) are defined: a set of exclusive, "binned" SRs, to maximise model-dependent exclusion sensitivity, and a set of "inclusive" SRs, to be used for model independent results. The definitions of these regions are provided in Table 2. Each SR is identified by the lepton flavour combination (DF or SF), $n_{\text{non-}b\text{-tagged jets}}$ (-0J,-1J) and the range of the m_{T2} interval.

6 Background estimation and validation

The SM backgrounds can be classified into irreducible backgrounds, from processes with prompt leptons and genuine $E_{\mathrm{T}}^{\mathrm{miss}}$ from neutrinos, and reducible backgrounds, which contain one or more FNP leptons. The main irreducible backgrounds in this search come from SM diboson (WW,WZ,ZZ) and top ($t\bar{t}$ and Wt) production. These are estimated using MC simulation but normalised using a simultaneous likelihood fit to data (as described in Section 8) in dedicated control regions (CRs). These are designed to be enriched in the particular background process under study while remaining kinematically similar to the SRs. The normalizations of these backgrounds are then validated in a set of validation regions (VRs), which are not used to constrain the fit, but are used to verify good agreement between data and predictions in regions of the parameter space kinematically close to the SRs. Three CRs are used, as defined in Table 3: CR-WW, targeting WW production; CR-top, targeting $t\bar{t}$ and single top, which are normalised by using a single normalisation parameter in the likelihood fit to the data; CR-VZ, targeting WZ and ZZ, which are normalised by using a single normalisation parameter in the likelihood fit to the data, as well.

The number of observed events in each CR, as well as the predicted yield of each SM process are reported in Table 4. For backgrounds whose normalization is extracted by the likelihood fit, the yield expected from the MC before the fit is also reported. After the fit, the total number of predicted events in the CRs

[3] The transverse mass is defined by $m_{\mathrm{T}} = \sqrt{2|\mathbf{p}_{\mathrm{T},1}||\mathbf{p}_{\mathrm{T},2}|(1-\cos(\Delta\phi))}$, where $\Delta\phi$ is the angle between the particles with transverse momenta $\mathbf{p}_{\mathrm{T},1}$ and $\mathbf{p}_{\mathrm{T},2}$

Signal region (SR)	SR-DF-0J	SR-DF-1J	SR-SF-0J	SR-SR-1J
$n_{\text{non-}b\text{-tagged jets}}$	= 0	= 1	= 0	= 1
$\lvert m_{\ell\ell} - m_Z \rvert$ [GeV]	–		>30	
$E_{\mathrm{T}}^{\mathrm{miss}}$ [GeV]	>110			
$E_{\mathrm{T}}^{\mathrm{miss}}$ significance	>10			
Binned SRs				
m_{T2} [GeV]	∈ [100,105]			
	∈ [105,110]			
	∈[110,120]			
	∈[120,140]			
	∈[140,160]			
	∈[160,180]			
	∈[180,220]			
	∈ [220, ∞]			
Inclusive SRs				
m_{T2} [GeV]	∈ [100, ∞]			
	∈ [160, ∞]			
	∈ [100, 120]			
	∈ [120, 160]			

Table 2: The definitions of the binned and inclusive signal regions. Relevant kinematic variables are defined in the text. The bins labelled "DF"or "SF" refer to signal regions with different-flavour or same-flavour lepton pair combinations, respectively.

Region	CR-VZ	CR-WW	CR-top
Lepton flavour	SF	DF	DF
$n_{b\text{-tagged jets}}$	= 0	= 0	= 1
$n_{\text{non-}b\text{-tagged jets}}$	= 0	= 0	= 0
m_{T2} [GeV]	> 120	∈ [60,65]	> 100
$E_{\mathrm{T}}^{\mathrm{miss}}$ [GeV]	> 110	> 60	> 110
$E_{\mathrm{T}}^{\mathrm{miss}}$ significance	> 10	> 5	> 5
$\lvert m_{\ell\ell} - m_Z \rvert$ [GeV]	< 30	–	–

Table 3: Control region definitions for extracting normalisation factors for the dominant background processes. "DF" or "SF" refer to regions with different-flavour or same-flavour lepton pair combinations, respectively.

matches the data by construction. The shape of kinematic distributions is well reproduced by the Monte Carlo in each CR. The m_{T2} distribution in CR-VZ and CR-top is shown in Figure 2.

The definitions of the VRs used in the analysis are provided in Table 5. For the WW background two validation regions are considered (VR-WW-0J and VR-WW-1J), according to the multiplicity of non-b-tagged jets in the event. As contributions from top backgrounds in VR-WW-0J and VR-WW-1J are not negligible, two VRs are defined for this background. VR-top-low requires the same m_{T2} range as VR-WW-0J and VR-WW-1J, this allowing the modelling of top quark production at lower values of m_{T2} to be validated. VR-top-high requires $m_{\mathrm{T2}} > 100$ GeV and provides validation in the high m_{T2} region where the SRs are defined.

Region	CR-VZ	CR-WW	CR-top
Observed events	487	1480	99
Fitted backgrounds	486 ± 22	1480 ± 40	99 ± 10
Fitted WW	11.3 ± 1.6	1020 ± 80	3.5 ± 1.9
Fitted WZ	114 ± 6	21.6 ± 1.8	0.23 ± 0.09
Fitted ZZ	353 ± 17	0.8 ± 0.1	–
Fitted $t\bar{t}$	$1.2^{+1.3}_{-1.2}$	270 ± 50	81 ± 9
Fitted single top	–	144 ± 23	9.2 ± 1.8
FNP	–	22.0 ± 2.5	3.34 ± 0.32
Other backgrounds	7.4 ± 3.4	1.4 ± 1.1	1.28 ± 0.15
MC exp. WW	8.5	762	2.6
MC exp. WZ	92	17.2	0.18
MC exp. ZZ	282	0.65	–
MC exp. $t\bar{t}$	1.1	256	76
MC exp. single top	–	134	8.6

Table 4: Observed events and predicted background yields from the fit for the CRs. For backgrounds whose normalization is extracted by the fit, the yield expected from the MC before the fit is also reported. The background denoted as "Other" in the Table includes the non-dominant background sources for this analysis, i.e. Z+jets, $t\bar{t}$ +V, Higgs and Drell-Yan events.

In order to obtain CRs and VRs of reasonable purity in WW production, CR-WW-0J and CR-WW-1J all require lower m_{T2} values than the SRs. To validate the tails of the m_{T2} distribution, a method similar to the one described in Ref. [17] is used. Three-lepton events emulating WZ processes are selected by requiring the absence of light jets and the presence of one same-flavour opposite-sign (SFOS) lepton pair whose invariant mass is consistent with that of the Z-boson ($|m_{\ell\ell} - m_Z| < 10$ GeV). To avoid overlaps with portions of the phase space relevant for other searches, three-lepton events are also required to satisfy $E_{\mathrm{T}}^{\mathrm{miss}} \in [40, 120]$ GeV. The transverse momentum of the lepton in the SFOS pair that has the same charge as the remaining lepton is added to the $\mathbf{p}_{\mathrm{T}}^{\mathrm{miss}}$ vector, to mimic a neutrino. The m_{T2} value can then be calculated using the remaining two leptons in the event. With this selection, good shape agreement for the m_{T2} distribution is observed between data and MC, and no additional systematic uncertainty is applied to the WW background at high m_{T2} values.

Sub-dominant irreducible background contributions come from SM processes such as Z+jets, Drell-Yan, $t\bar{t}$ +V and Higgs. These processes, jointly referred to as "Other backgrounds" are estimated directly from MC simulation using the samples described in Section 3. The remaining background from FNP leptons is estimated from data using the matrix method (MM) [58]. This method considers two types of lepton identification criteria: so-called "signal" leptons, corresponding to leptons passing the full analysis selection, and so-called "baseline" leptons, as defined in Section 4. Probabilities for prompt leptons satisfying the baseline selection to also satisfy the signal selection are measured as a function of lepton p_{T} and η in dedicated regions enriched in Z-boson processes; similar probabilities for FNP leptons are measured in events dominated by leptons from heavy flavour decays and photon conversions. These probabilities are used in the matrix method to extract data-driven estimates for the FNP lepton background in the CRs, VRs, and SRs, looking at the numbers of observed events containing a pair of baseline leptons in which one of the two leptons, both or none of them passes the signal selection in a given region. The observed number of events and the predicted background in each VR are reported in Table 6. For

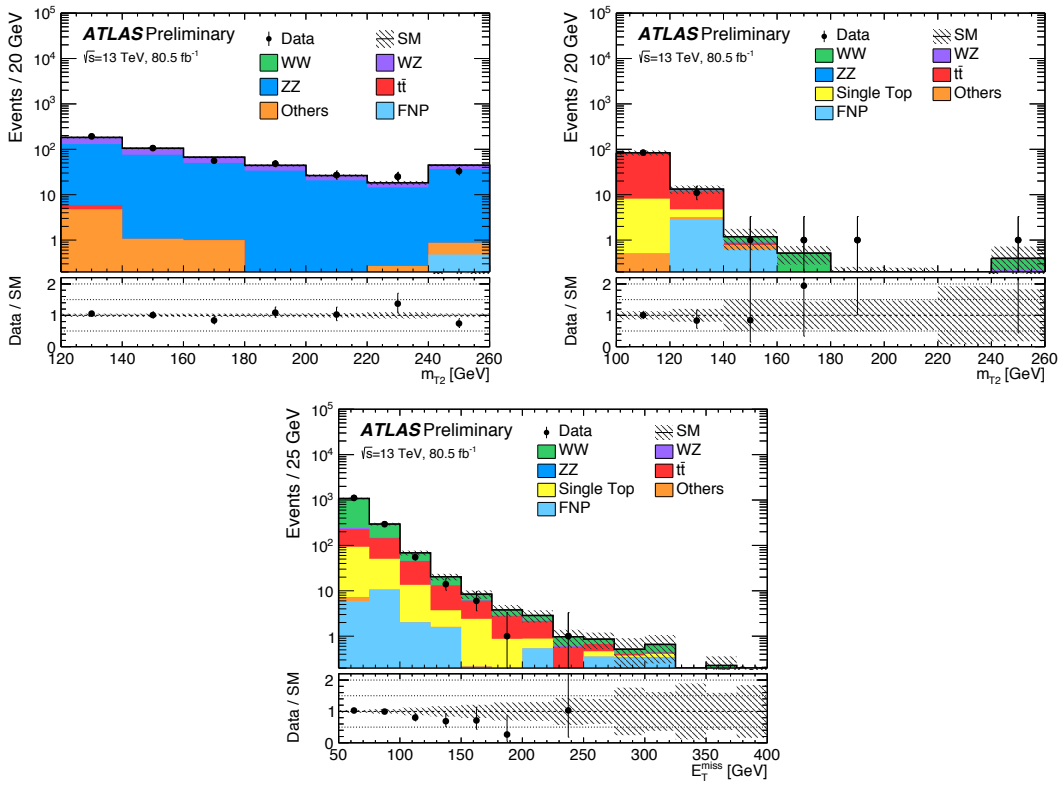

Figure 2: Distributions of m_{T2} for CR-VZ (left) and CR-top (right) and distribution of $E_{\mathrm{T}}^{\mathrm{miss}}$ for CR-WW (bottom) for data and the estimated SM backgrounds. The normalization factors extracted from the corresponding CRs are used to rescale the $t\bar{t}$, single top, WW, WZ and ZZ backgrounds. The FNP background is calculated using the data-driven matrix method. The uncertainty band includes all systematic and statistical sources and the final bin in each histogram includes the overflow.

backgrounds whose normalization is extracted by the fit, the expected yield from simulated MC samples before the fit is also reported. Figure 3 shows a selection of kinematic distributions for data and the estimated SM background in the validation regions defined in Table 5. Good agreement is observed in all regions.

Region	VR-WW-0J	VR-WW-1J	VR-VZ	VR-top-low	VR-top-high
Lepton flavour	DF	DF	SF	DF	DF
$n_{b\text{-tagged jets}}$	= 0	= 0	= 0	= 1	= 1
$n_{\text{non-}b\text{-tagged jets}}$	= 0	= 1	= 0	= 0	= 1
m_{T2} [GeV]	$\in$ [65,100]	$\in$[65,100]	$\in$[100,120]	$\in$[80,100]	> 100
$E_{\mathrm{T}}^{\mathrm{miss}}$ [GeV]	> 60	> 60	> 110	> 110	> 110
$E_{\mathrm{T}}^{\mathrm{miss}}$ significance	> 5	> 5	> 10	> 5	> 5
$\lvert m_{\ell\ell} - m_Z \rvert$ [GeV]	–	–	< 30	–	–

Table 5: Validation region definitions used to study the modelling of the SM backgrounds. "DF" or "SF" refer to regions with different-flavour or same-flavour lepton pair combinations, respectively.

Region	VR-WW-0J	VR-WW-1J	VR-VZ	VR-top-low	VR-top-high
Observed events	3873	3509	265	526	121
Fitted background	3970 ± 170	4000 ± 700	260 ± 21	620 ± 100	143 ± 29
Fitted WW	2210 ± 190	1360 ± 150	11.0 ± 1.3	6 ± 5	$2.9^{+3.0}_{-2.9}$
Fitted WZ	49 ± 4	36 ± 4	61 ± 5	0.17 ± 0.13	$0.18^{+0.22}_{-0.18}$
Fitted ZZ	2.97 ± 0.28	1.28 ± 0.21	161 ± 14	–	–
Fitted $t\bar{t}$	1076 ± 200	2000 ± 600	6 ± 4	520 ± 90	118 ± 26
Fitted single top	570 ± 100	640 ± 160	1.7 ± 1.3	87 ± 13	11.5 ± 2.9
FNP	47 ± 6	36 ± 6	–	6.9 ± 0.7	5.8 ± 0.5
Other backgrounds	9 ± 3	5 ± 2	17.7 ± 6.6	–	3.4 ± 0.4
MC exp. WW	1660	1020	8.2	4.5	2.2
MC exp. WZ	39	28	48	0.13	0.14
MC exp. ZZ	2.35	1.01	128	–	–
MC exp. $t\bar{t}$	1000	1800	6	490	110
MC exp. single top	540	600	1.6	81	10.8

Table 6: Observed events and predicted background yields from the fit for the VRs. For backgrounds whose normalization is extracted by the fit, the yield expected from the MC before the fit is also reported. The background denoted as "Other" includes the non-dominant background sources for this analysis, i.e. Z+jets, $t\bar{t}$ +V, Higgs and Drell-Yan events. A "–" symbol indicates that the background contribution is negligible.

7 Systematic uncertainties

All relevant sources of experimental and theoretical systematic uncertainty affecting the SM background estimates and the signal predictions are included in the profile likelihood fit described in Section 8. The dominant sources of systematic uncertainty are related to the jet energy scale (JES) and jet energy resolution (JER), the b-jet identification efficiency and the theory uncertainties in the MC modelling. In addition, the re-weighting procedure applied to simulation to match the distribution of the number of reconstructed vertices observed in data results in a non negligible contribution to the total systematic uncertainty. The statistical uncertainty of the simulated event samples is also accounted for in the analysis.

The JES and JER uncertainties are considered as a function of jet p_{T} and η, the pile-up conditions and the jet flavour composition of the selected jet sample. They are derived using a combination of data and simulation, through measurements of the jet response balance in dijet, Z+jets and γ+jets events [59, 60]. An additional uncertainty on $\mathbf{p}_{\mathrm{T}}^{\mathrm{miss}}$ comes from the soft term's resolution and scale [61]. Uncertainties on the scale factors applied to the MC samples to account for differences between data and simulation in the b-jet identification efficiency are also included. The remaining experimental systematic uncertainties, such as those in the lepton reconstruction efficiency, lepton energy scale and lepton energy resolution and differences of the trigger efficiencies in data and simulation, are included and were found to be of few per mille in all channels.

Several sources of theoretical uncertainty on the modelling of the dominant MC backgrounds are considered. Uncertainties in the MC modelling of diboson events are estimated by varying the PDF sets as well as the renormalization, factorization and merging scales used to generate the samples. For $t\bar{t}$ production, uncertainties from the parton shower simulation are accounted for by comparing samples with Powheg interfaced to either Pythia or Herwig++. Another source of uncertainty comes from the model-

Region	SR-DF-0J [100, ∞]	SR-DF-1J [100, ∞]	SR-SF-0J [100, ∞]	SR-SF-1J [100, ∞]
Total background expectation	101	83	120	113
Total background systematic	11.8%	17.7%	7.4%	11.0%
MC statistical uncertainties	4%	5%	4%	5%
WW normalization	6%	5%	4%	3%
VZ normalization	< 1%	< 1%	2%	2%
$t\bar{t}$ normalization	4%	6%	2%	4%
Diboson theoretical uncertainties	3%	10%	5%	4%
Top theoretical uncertainties	9%	8%	2%	5%
$E_{\mathrm{T}}^{\mathrm{miss}}$ modelling	2%	2%	2%	2%
Jet energy scale	1%	8%	1%	5%
Jet energy resolution	1%	4%	1%	3%
Pile-up reweighting	1%	1%	1%	2%
b-tagging	< 1%	6%	< 1%	4%
Lepton modelling	1%	< 1%	< 1%	1%
FNP	< 1%	< 1%	< 1%	< 1%

Table 7: Breakdown of the dominant systematic uncertainties on background estimates in the inclusive SRs requiring m_{T2}>100 GeV. Note that the individual uncertainties can be correlated, and do not necessarily add up quadratically to the total background uncertainty. The percentages show the size of the uncertainty relative to the total expected background. "Top theoretical uncertainties" refers to $t\bar{t}$ theoretical uncertainties and the uncertainty associated to $Wt - t\bar{t}$ interference added quadratically.

ling of initial and final state radiation (ISR/FSR). Finally, for single top Wt production an uncertainty is associated to the treatment of the interference between the Wt and $t\bar{t}$ samples. This compares the nominal sample generated using the diagram removal method to a sample generated using the diagram subtraction method [62].

For the matrix method estimate of the FNP background, systematic uncertainties are assigned to account for possible differences in FNP lepton composition between the regions used to derive the FNP yields and the ones defined to validate the method itself.

A summary of the impact of the systematic uncertainties, after performing the profile likelihood fit, on the inclusive SRs with $m_{\mathrm{T2}} > 100$ GeV, is shown in Table 7. For the binned SRs defined in Table 2, the uncertainties associated with limited MC statistics are higher, ranging between 6-20%.

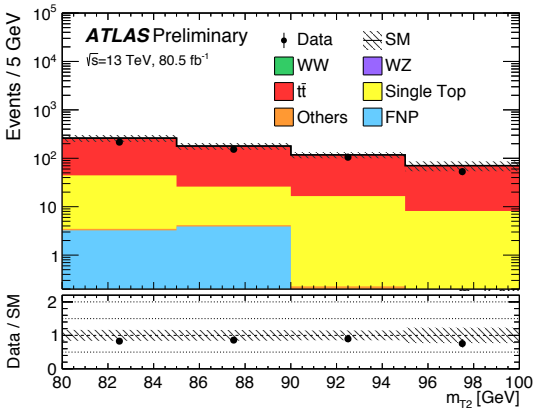

(a) m_{T2} distribution in VR-top-low

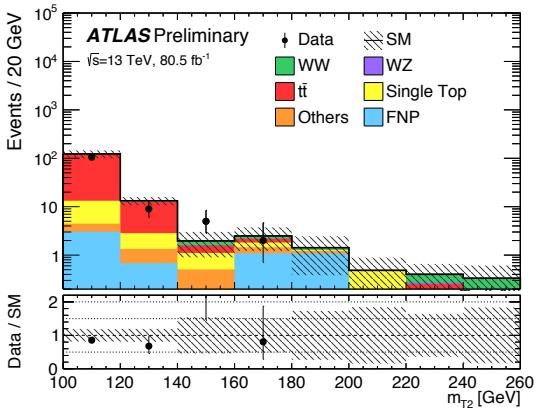

(b) m_{T2} distribution in VR-top-high

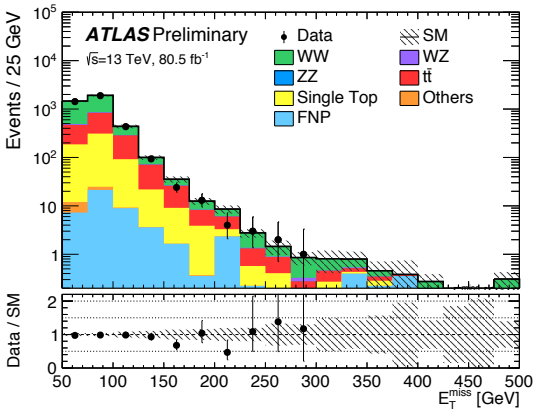

(c) $E_{\mathrm{T}}^{\mathrm{miss}}$ distribution in VR-WW-0J

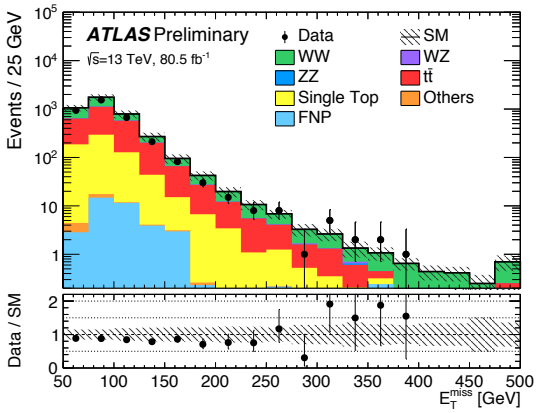

(d) $E_{\mathrm{T}}^{\mathrm{miss}}$ distribution in VR-WW-1J

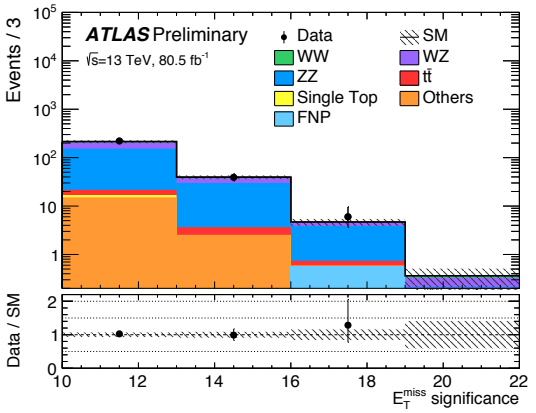

(e) $E_{\mathrm{T}}^{\mathrm{miss}}$ significance distribution in VR-VZ

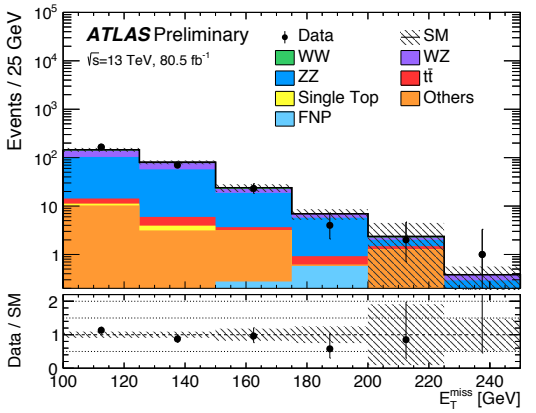

(f) $E_{\mathrm{T}}^{\mathrm{miss}}$ distribution in VR-VZ

Figure 3: Distributions of m_{T2} in VR-top-low (a) and VR-top-high (b), $E_{\mathrm{T}}^{\mathrm{miss}}$ in VR-WW-0J (c) and VR-WW-1J (d), and $E_{\mathrm{T}}^{\mathrm{miss}}$ significance (e) and $E_{\mathrm{T}}^{\mathrm{miss}}$ (f) in VR-VZ, for data and the estimated SM backgrounds. The normalization factors extracted from the corresponding CRs are used to rescale the $t\bar{t}$, single top, WW, WZ and ZZ backgrounds. The FNP background is calculated using the data-driven matrix method. The uncertainty band includes all systematic and statistical sources and the last bin includes the overflow.

8 Results

The statistical interpretation of the final results is performed using the HistFitter framework [63]. A simultaneous likelihood fit of the CRs and the SRs is performed. The likelihood is a product of Poisson probability density functions describing the observed number of events in each CR/SR and Gaussian distributions that constrain the nuisance parameters associated with the systematic uncertainties. Poisson distributions are used for MC statistical uncertainties. When relevant, correlations of systematic uncertainties across samples are accounted for in the fit configuration by using the same nuisance parameter.

Firstly, a background-only fit which uses data in the CRs only is performed to constrain the nuisance parameters of the likelihood function, which include the normalisation factors and parameters associated with the systematic uncertainties. The results of the background-only fit are used to assess agreement between the data and background estimates in the validation regions. Good agreement is observed, as shown in Section 6.

The results of the background-only fit together with the observed data for the binned SRs are shown in Figure 4. The observed and the predicted number of background events in the inclusive SRs are reported in Tables 8 and 9. Figure 5 shows the m_{T2} distribution for the data and the estimated SM backgrounds for events in the SRs.

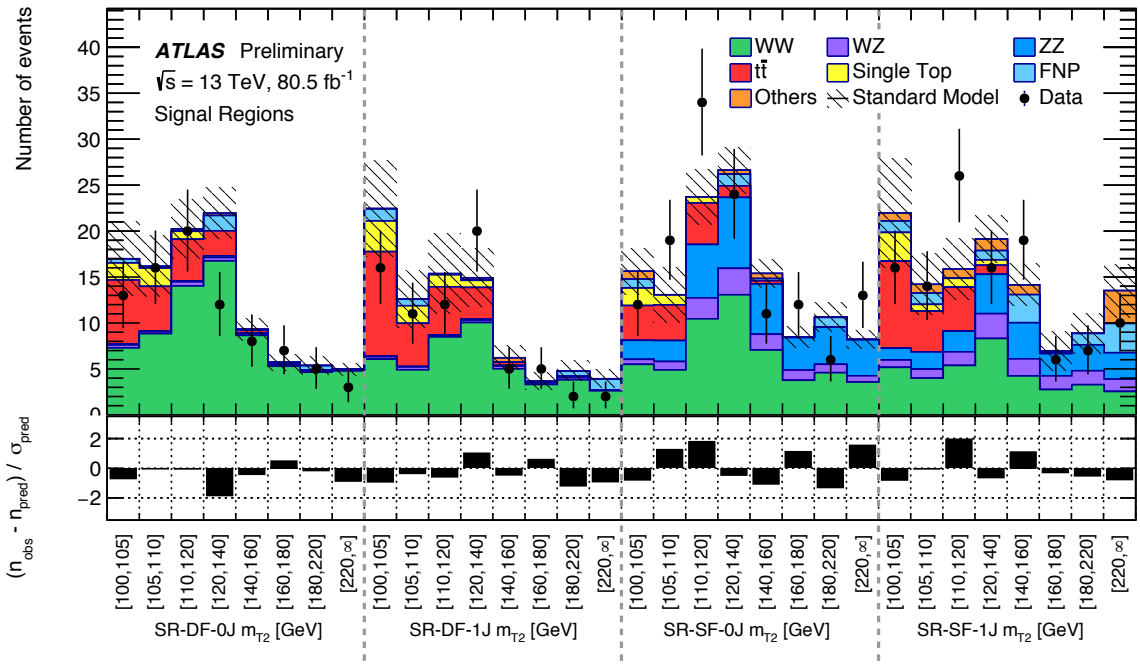

Figure 4: The upper panel reports the observed number of events and the expected SM backgrounds obtained using the background-only fit for each of the binned SRs defined in Table 2. The shaded band represents the uncertainty on the expected SM background. The lower panel reports the difference between the observation and the predicted background, divided by the total uncertainty.

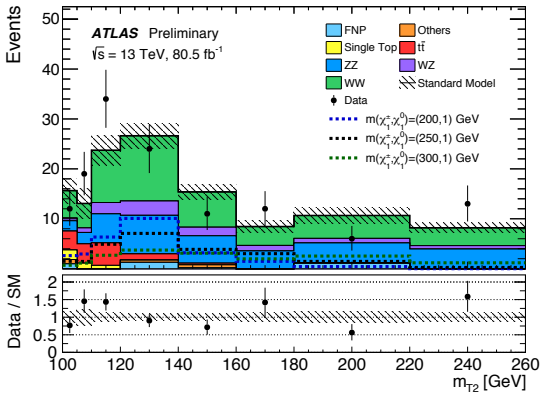

(a) m_{T2} distribution in SRSF-0J

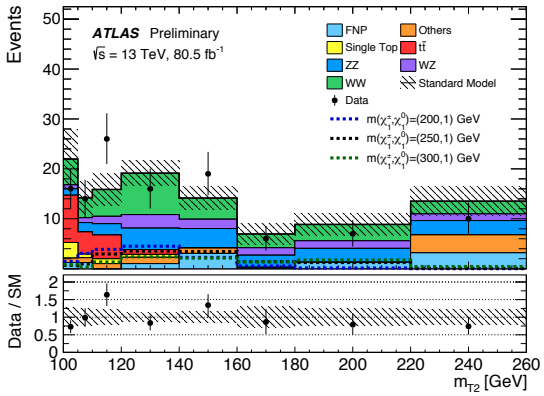

(b) m_{T2} distribution in SRSF-1J

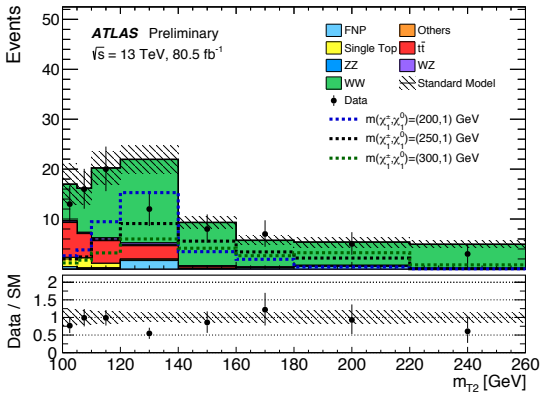

(c) m_{T2} distribution in SRDF-0J

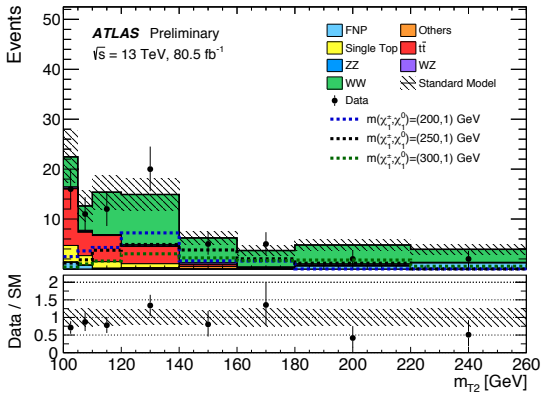

(d) m_{T2} distribution in SRDF-1J

Figure 5: Distributions of m_{T2} in SRSF-0J (a), SR-SF-1J (b), SRDF-0J (c) and SRDF-1J (d), for data and the estimated SM backgrounds. The normalization factors extracted from the corresponding CRs are used to rescale the $t\bar{t}$, single top, WW, WZ and ZZ backgrounds. The FNP background is calculated using the data-driven matrix method. The uncertainty band includes all systematic and statistical sources and the last bin includes the overflow. Distributions for three benchmark signal points are overlaid for comparison.

Region	SR-SF-0J [100, ∞]	SR-SF-0J [160, ∞]	SR-SF-0J [100, 120]	SR-SF-0J [120, 160]
Observed events	131	31	65	35
Fitted background	119.67 ± 9.0	27.1 ± 2.7	50.9 ± 5.7	42.3 ± 3.4
Fitted WW	53.2 ± 7.7	12.0 ± 2.0	21.0 ± 3.3	20.3 ± 2.9
Fitted WZ	11.09 ± 0.74	2.72 ± 0.26	3.75 ± 0.44	4.62 ± 0.35
Fitted ZZ	35.1 ± 2.4	11.6 ± 1.0	10.2 ± 1.0	13.28 ± 0.95
Fitted $t\bar{t}$	13.9 ± 3.2	$0.02^{+0.04}_{-0.02}$	12.3 ± 2.9	1.61 ± 0.66
Fitted single top	3.7 ± 2.2	–	3.7 ± 2.2	$0.00^{+0.15}_{-0.00}$
FNP	2.03 ± 0.21	0.82 ± 0.11	$0.00^{+0.01}_{-0.00}$	1.51 ± 0.12
Other backgrounds	$0.6^{+1.7}_{-0.6}$	$0.00^{+0.30}_{-0.00}$	$0.00^{+1.5}_{-0.00}$	1.02 ± 0.19
$S^{0.95}_{\text{obs}}$	42.0	16.4	34.2	11.5
$S^{0.95}_{\text{exp}}$	$31.1^{+12.5}_{-8.1}$	$14.7^{+4.0}_{-5.4}$	$22.0^{+6.6}_{-8.0}$	$15.8^{+5.8}_{-4.1}$
$\sigma^{0.95}_{\text{obs}}$ [fb]	0.52	0.21	0.43	0.14
p_0	0.17	0.23	0.05	0.50

Region	SR-SF-1J [100, ∞]	SR-SF-1J [160, ∞]	SR-SF-1J [100, 120]	SR-SF-1J [120, 160]
Observed events	114	23	56	35
Fitted background	114 ± 13	29 ± 5	51.7 ± 10.0	33 ± 4
Fitted WW	36 ± 5	8.6 ± 1.7	14.6 ± 2.4	12.6 ± 1.9
Fitted WZ	12.2 ± 1.7	4.38 ± 0.80	3.28 ± 0.47	4.59 ± 0.75
Fitted ZZ	21.8 ± 3.0	8.1 ± 1.5	5.43 ± 0.95	8.3 ± 1.3
Fitted $t\bar{t}$	20.0 ± 7.5	$0.15^{+0.17}_{-0.15}$	19 ± 7	0.99 ± 0.95
Fitted single top	5.4 ± 3.5	–	4.9 ± 3.2	0.59 ± 0.41
FNP	10.44 ± 0.83	4.58 ± 0.68	1.79 ± 0.16	4.07 ± 0.45
Other backgrounds	8.0 ± 2.7	2.8 ± 1.5	2.9 ± 1.8	2.34 ± 0.89
$S^{0.95}_{\text{obs}}$	32.3	11.6	29.0	18.4
$S^{0.95}_{\text{exp}}$	$30.9^{+13.2}_{-7.4}$	$14.1^{+5.9}_{-3.2}$	$27.5^{+9.1}_{-8.3}$	$17.2^{+3.5}_{-6.9}$
$\sigma^{0.95}_{\text{obs}}$ [fb]	0.40	0.15	0.36	0.23
p_0	0.47	0.50	0.35	0.39

Table 8: Observed events and predicted background yields from the fit for the SF inclusive SRs. The model independent upper limits on the observed and expected number of beyond the SM events $S^{0.95}_{\text{obs/exp}}$ and the effective beyond the SM cross-section $\sigma^{0.95}_{\text{obs}}$ are also reported. The last row reports the p_0-value of the SM-only hypothesis. For SRs where the data yield is smaller than expected, the p-value is truncated at 0.50. The background denoted as "Other" in the Table includes the non-dominant background sources for this analysis, i.e. Z+jets, $t\bar{t}+V$, Higgs and Drell-Yan events. A "–" symbol indicates that the background contribution is negligible.

Region	SR-DF-0J [100, ∞]	SR-DF-0J [160, ∞]	SR-DF-0J [100, 120]	SR-DF-0J [120, 160]
Observed events	84	15	49	20
Fitted background	100.8 ± 11.9	16.1 ± 2.0	53.4 ± 9.0	31.5 ± 3.5
Fitted WW	70.7 ± 7.5	14.8 ± 1.9	30.3 ± 3.5	25.6 ± 3.0
Fitted WZ	2.02 ± 0.25	0.47 ± 0.07	0.98 ± 0.21	0.58 ± 0.10
Fitted ZZ	0.66 ± 0.08	0.17 ± 0.04	$0.25^{+0.25}_{-0.25}$	0.23 ± 0.04
Fitted $t\bar{t}$	19.6 ± 9.3	–	16.6 ± 7.9	3.1 ± 1.5
Fitted single top	4.8 ± 2.6	–	4.8 ± 2.6	$0.00^{+0.14}_{-0.00}$
FNP	2.19 ± 0.33	0.53 ± 0.15	$0.00^{+0.05}_{-0.00}$	1.75 ± 0.17
Other backgrounds	0.81 ± 0.18	0.05 ± 0.01	0.47 ± 0.17	0.28 ± 0.07
$S^{0.95}_{\text{obs}}$	23.1	9.2	20.9	7.4
$S^{0.95}_{\text{exp}}$	$33.1^{+11.1}_{-8.7}$	$9.7^{+4.0}_{-2.8}$	$23.4^{+9.1}_{-6.4}$	$13.6^{+5.1}_{-3.7}$
$\sigma^{0.95}_{\text{obs}}$ [fb]	0.29	0.12	0.26	0.09
p_0	0.50	0.48	0.50	0.50

Region	SR-DF-1J [100, ∞]	SR-DF-1J [160, ∞]	SR-DF-1J [100, 120]	SR-DF-1J [120, 160]
Observed events	73	9	39	25
Fitted background	83.5 ± 14.6	12.2 ± 2.5	50.6 ± 10.7	21.2 ± 4.0
Fitted WW	45 ± 10	9.8 ± 2.3	19.6 ± 4.8	15.2 ± 3.5
Fitted WZ	1.83 ± 0.45	0.50 ± 0.15	0.77 ± 0.24	0.56 ± 0.17
Fitted ZZ	0.60 ± 0.15	0.29 ± 0.09	0.14 ± 0.04	0.17 ± 0.05
Fitted $t\bar{t}$	25.2 ± 8.4	–	21.4 ± 7.3	3.8 ± 1.6
Fitted single top	7.4 ± 4.1	–	6.6 ± 3.7	0.78 ± 0.46
FNP	2.77 ± 0.27	1.48 ± 0.20	1.90 ± 0.16	$0.00^{+0.01}_{-0.00}$
Other backgrounds	1.11 ± 0.18	0.15 ± 0.04	0.21 ± 0.07	0.75 ± 0.10
$S^{0.95}_{\text{obs}}$	24.0	6.8	17.8	14.4
$S^{0.95}_{\text{exp}}$	$29.2^{+11.5}_{-8.0}$	$8.4^{+4.2}_{-2.6}$	$25.8^{+9.3}_{-8.3}$	$13.4^{+4.3}_{-2.1}$
$\sigma^{0.95}_{\text{obs}}$ [fb]	0.30	0.09	0.22	0.18
p_0	0.50	0.50	0.50	0.23

Table 9: Observed events and predicted background yields from the fit for the DF inclusive SRs. The model independent upper limits on the observed and expected number of beyond the SM events $S^{0.95}_{\text{obs/exp}}$ and the effective beyond the SM cross-section $\sigma^{0.95}_{\text{obs}}$ are also reported. The last row reports the p_0-value of the SM-only hypothesis. For SRs where the data yield is smaller than expected, the p-value is truncated at 0.50. The background denoted as "Other" in the Table includes the non-dominant background sources for this analysis, i.e. Z+jets, $t\bar{t}+V$, Higgs and Drell-Yan events. A "–" symbol indicates that the background contribution is negligible.

No significant deviation from the SM expectations is observed in any of the considered SRs, as shown in Figures 4 and 5. The CL_s prescription [64] is used to calculate 95% confidence level (CL) exclusion limits as a function of the $\tilde{\chi}_1^{\pm}$ and the $\tilde{\chi}_1^0$ masses for the simplified model shown in Figure 1. All of the exclusive regions defined in Table 2 are statistically combined when performing the profile likelihood fit. The results are shown in Figure 6. For a massless $\tilde{\chi}_1^0$, $\tilde{\chi}_1^{\pm}$ masses up to 410 GeV are excluded at 95% CL.

Model-independent upper limits are set on the visible signal cross-section $\sigma_{\text{obs}}^{0.95}$, defined as cross-section times acceptance times efficiency, of beyond the SM physics processes. They are derived in each SR by performing a fit which includes the observed yield in the SR as a constraint, and a free signal yield in the SR as an additional process. The observed ($S_{\text{obs}}^{0.95}$) and expected ($S_{\text{exp}}^{0.95}$) number of events from processes beyond the SM in the inclusive SRs defined in Section 5 are calculated.The p_0-values, which represent the probability of the SM background alone to fluctuate to the observed number of events or higher, are also provided and are capped at $p_0 = 0.50$. These results are presented in Tables 8 and 9 for the SF and DF inclusive SRs respectively.

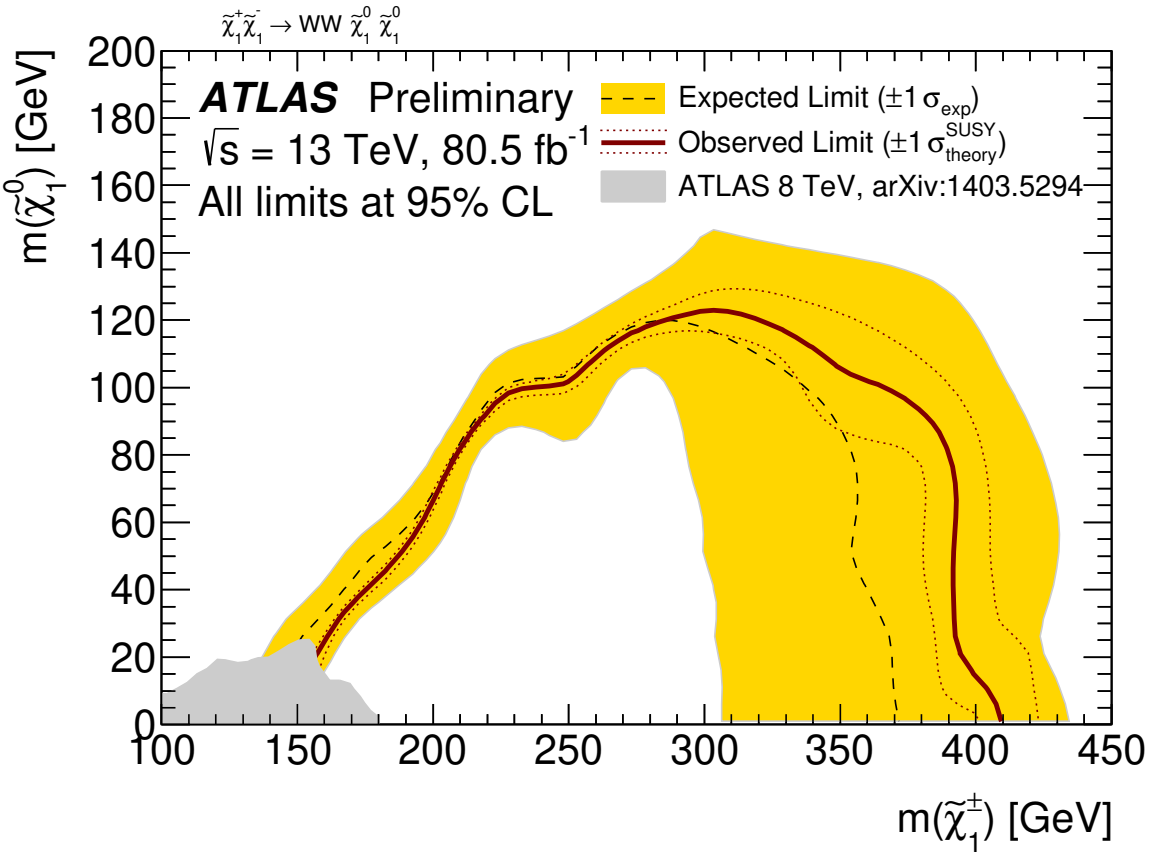

Figure 6: Observed and expected exclusion limits on SUSY simplified models for chargino-pair production with W-boson mediated decays. All limits are computed at 95% confidence level. The observed limits obtained from ATLAS in Run-1 are also shown [16].

9 Conclusion

A search for the electroweak production of chargino pairs $\tilde{\chi}_1^+\tilde{\chi}_1^-$ decaying via W-bosons into final states with exactly two opposite-sign leptons and missing transverse momentum is presented. The analysis uses 80.5 fb^{-1} of $\sqrt{s}$ = 13 TeV proton–proton collisions recorded by the ATLAS detector at the Large Hadron Collider between 2015 and 2017. No significant excess above the SM expectation is observed in any of the signal regions considered and the results are used to calculate exclusion limits. For a massless $\tilde{\chi}_1^0$, $\tilde{\chi}_1^\pm$ masses up to 410 GeV are excluded at 95% confidence level. These results significantly improve upon previous exclusion limits [16, 17] for the same scenario.

References

[1] Yu. A. Golfand, *Extension of the Algebra of Poincare Group Generators and Violation of p Invariance*, JETP Lett. **13** (1971) 323, [Pisma Zh. Eksp. Teor. Fiz. **13** (1971) 452].

[2] D. V. Volkov and V. P. Akulov, *Is the Neutrino a Goldstone Particle?*, Phys. Lett. B **46** (1973) 109.

[3] J. Wess and B. Zumino, *Supergauge Transformations in Four-Dimensions*, Nucl. Phys. B **70** (1974) 39.

[4] J. Wess and B. Zumino, *Supergauge Invariant Extension of Quantum Electrodynamics*, Nucl. Phys. B **78** (1974) 1.

[5] S. Ferrara and B. Zumino, *Supergauge Invariant Yang-Mills Theories*, Nucl. Phys. B **79** (1974) 413.

[6] A. Salam and J. A. Strathdee, *Supersymmetry and Nonabelian Gauges*, Phys. Lett. B **51** (1974) 353.

[7] N. Sakai, *Naturalness in Supersymmetric Guts*, Z. Phys. C **11** (1981) 153.

[8] S. Dimopoulos, S. Raby and F. Wilczek, *Supersymmetry and the Scale of Unification*, Phys. Rev. D **24** (1981) 1681.

[9] L. E. Ibanez and G. G. Ross, *Low-Energy Predictions in Supersymmetric Grand Unified Theories*, Phys. Rev. B **105** (1981) 439.

[10] S. Dimopoulos and H. Georgi, *Softly Broken Supersymmetry and SU(5)*, Nucl. Phys. B **193** (1981) 150.

[11] G. R. Farrar and P. Fayet, *Phenomenology of the Production, Decay, and Detection of New Hadronic States Associated with Supersymmetry*, Phys. Lett. B **76** (1978) 575.

[12] H. Goldberg, *Constraint on the Photino Mass from Cosmology*, Phys. Rev. Lett. **50** (1983) 1419, [Erratum: Phys. Rev. Lett.103,099905(2009)].

[13] J. R. Ellis, J. S. Hagelin, D. V. Nanopoulos, K. A. Olive and M. Srednicki, *Supersymmetric Relics from the Big Bang*, Nucl. Phys. B **238** (1984) 453.

[14] ATLAS Collaboration, *Search for squarks and gluinos in final states with jets and missing transverse momentum using* 36 fb^{-1} *of* $\sqrt{s}$ = 13 *TeV pp collision data with the ATLAS detector*, Phys. Rev. D **97** (2018) 112001, arXiv: 1712.02332 [hep-ph].

[15] J. Alwall, P. Schuster and N. Toro, *Simplified Models for a First Characterization of New Physics at the LHC*, Phys. Rev. D **79** (2009) 075020, arXiv: 0810.3921 [hep-ph].

[16] ATLAS Collaboration, *Search for direct production of charginos, neutralinos and sleptons in final states with two leptons and missing transverse momentum in pp collisions at* $\sqrt{s}$ = 8 *TeV with the ATLAS detector*, JHEP **05** (2014) 071, arXiv: 1403.5294 [hep-ex].

[17] CMS Collaboration, *Search for chargino pair production and top squark pair production in final states with two leptons in proton-proton collisions at* $\sqrt{s}$ = 13 TeV, CMS-PAS-SUS-17-010, 2018, URL: https://cds.cern.ch/record/2309556.

[18] ATLAS Collaboration, *The ATLAS Experiment at the CERN Large Hadron Collider*, JINST **3** (2008) S08003.

[19] ATLAS Collaboration, *ATLAS Pixel IBL: Stave Quality Assurance*, ATL-INDET-PUB-2014-006, 2014, URL: https://cds.cern.ch/record/1754509.

[20] ATLAS Collaboration, *Performance of the ATLAS Trigger System in 2015*, Eur. Phys. J. C **77** (2017) 317, arXiv: 1611.09661 [hep-ex].

[21] ATLAS Collaboration, *Luminosity determination in pp collisions at $\sqrt{s}$ = 8 TeV using the ATLAS detector at the LHC*, Eur. Phys. J. C **76** (2016) 653, arXiv: 1608.03953 [hep-ex].

[22] ATLAS Collaboration, *The ATLAS Simulation Infrastructure*, Eur. Phys. J. C **70** (2010) 823, arXiv: 1005.4568 [physics.ins-det].

[23] S. Agostinelli et al., *GEANT4: A Simulation toolkit*, Nucl. Instrum. Meth. A **506** (2003) 250.

[24] J. Alwall et al., *The automated computation of tree-level and next-to-leading order differential cross sections, and their matching to parton shower simulations*, JHEP **07** (2014) 079, arXiv: 1405.0301 [hep-ph].

[25] T. Sjöstrand, S. Mrenna and P. Z. Skands, *A Brief Introduction to PYTHIA 8.1*, Comput. Phys. Commun. **178** (2008) 852, arXiv: 0710.3820 [hep-ph].

[26] ATLAS Collaboration, *ATLAS Pythia 8 tunes to 7 TeV data*, ATL-PHYS-PUB-2014-021, 2014, URL: https://cds.cern.ch/record/1966419.

[27] R. D. Ball et al., *Parton distributions with LHC data*, Nucl. Phys. B **867** (2013) 244, arXiv: 1207.1303 [hep-ph].

[28] L. Lönnblad and S. Prestel, *Merging Multi-leg NLO Matrix Elements with Parton Showers*, JHEP **03** (2013) 166, arXiv: 1211.7278 [hep-ph].

[29] W. Beenakker, R. Hopker, M. Spira and P. Zerwas, *Squark and gluino production at hadron colliders*, Nucl. Phys. B. **492** (1997) 51, arXiv: hep-ph/9610490.

[30] A. Kulesza and L. Motyka, *Threshold resummation for squark-antisquark and gluino-pair production at the LHC*, Phys. Rev. Lett. **102** (2009) 111802, arXiv: 0807.2405 [hep-ph].

[31] A. Kulesza and L. Motyka, *Soft gluon resummation for the production of gluino-gluino and squark-antisquark pairs at the LHC*, Phys. Rev. D **80** (2009) 095004, arXiv: 0905.4749 [hep-ph].

[32] W. Beenakker, S. Brensing, M. Kramer, A. Kulesza, E. Laenen et al., *Soft-gluon resummation for squark and gluino hadroproduction*, JHEP **12** (2009) 041, arXiv: 0909.4418 [hep-ph].

[33] W. Beenakker, S. Brensing, M. Kramer, A. Kulesza, E. Laenen et al., *Squark and gluino hadroproduction*, Int. J. Mod. Phys. A **26** (2011) 2637, arXiv: 1105.1110 [hep-ph].

[34] C. Borschensky et al., *Squark and gluino production cross sections in pp collisions at $\sqrt{s}$ = 13, 14, 33 and 100 TeV*, Eur. Phys. J. C **74** (2014) 3174, arXiv: 1407.5066 [hep-ph].

[35] ATLAS Collaboration, *Summary of ATLAS Pythia 8 tunes*, ATL-PHYS-PUB-2012-003, 2012, URL: https://cds.cern.ch/record/1474107.

[36] A. D. Martin, W. J. Stirling, R. S. Thorne and G. Wat, *Parton distributions for the LHC*, Eur. Phys. J. C **63** (2009) 189, arXiv: 0901.0002 [hep-ph].

[37] S. Alioli, P. Nason, C. Oleari and E. Re, *A general framework for implementing NLO calculations in shower Monte Carlo programs: the POWHEG BOX*, JHEP **06** (2010) 043, arXiv: 1002.2581 [hep-ph].

[38] J. M. Campbell, R. K. Ellis, P. Nason and E. Re, *Top-pair production and decay at NLO matched with parton showers*, JHEP **04** (2015) 114, arXiv: 1412.1828 [hep-ph].

[39] P. Z. Skands, *Tuning Monte Carlo Generators: The Perugia Tunes*, Phys. Rev. D **82** (2010) 074018, arXiv: 1005.3457 [hep-ph].

[40] H.-L. Lai, M. Guzzi, J. Huston, Z. Li, P. M. Nadolsky et al., *New parton distributions for collider physics*, Phys. Rev. D **82** (2010) 074024, arXiv: 1007.2241 [hep-ph].

[41] T. Sjöstrand, S. Mrenna and P. Z. Skands, *PYTHIA 6.4 Physics and Manual*, JHEP **05** (2006) 026, arXiv: 0605.026 [hep-ph].

[42] G. Gleisberg et al., *Event generation with SHERPA 1.1*, JHEP **02** (2009) 007, arXiv: 0811.4622 [hep-ph].

[43] R. D. Ball et al., *Parton distributions with LHC data Run II*, JHEP **04** (2015) 040, arXiv: 1410.8849 [hep-ph].

[44] ATLAS Collaboration, *Measurements of the Z/γ^* boson transverse momentum distribution in pp collisions at $\sqrt{s}$ = 7 TeV with the ATLAS detector*, JHEP **09** (2014) 055, arXiv: 1406.3660 [hep-ph].

[45] J. Pumplin et al., *New Generation of Parton Distributions with Uncertainties from Global QCD Analysis*, JHEP **07** (2002) 012, arXiv: 0207.012 [hep-ph].

[46] ATLAS Collaboration, *Electron efficiency measurements with the ATLAS detector using the 2015 LHC proton–proton collision data*, ATLAS-CONF-2016-024, 2016, URL: https://cds.cern.ch/record/2157687.

[47] ATLAS Collaboration, *Muon reconstruction performance of the ATLAS detector in proton–proton collision data at $\sqrt{s}$ = 13 TeV*, Eur. Phys. J. C **76** (2016) 292, arXiv: 1603.05598 [hep-ex].

[48] ATLAS Collaboration, *Topological cell clustering in the ATLAS calorimeters and its performance in LHC Run 1*, Eur. Phys. J. C **77** (2017) 490, arXiv: 1603.02934 [hep-ex].

[49] M. Cacciari, G. P. Salam and G. Soyez, *The anti-k_t jet clustering algorithm*, JHEP **04** (2008) 063, arXiv: 0802.1189 [hep-ph].

[50] ATLAS Collaboration, *Jet energy scale measurements and their systematic uncertainties in proton–proton collisions at $\sqrt{s}$ = 13 TeV with the ATLAS detector*, Phys. Rev. D **96** (2017) 072002, arXiv: 1703.09665 [hep-ex].

[51] ATLAS Collaboration, *Tagging and suppression of pileup jets with the ATLAS detector*, ATLAS-CONF-2014-018, 2014, URL: https://cds.cern.ch/record/1700870.

[52] ATLAS Collaboration, *Selection of jets produced in* 13 *TeV proton–proton collisions with the ATLAS detector*, ATLAS-CONF-2015-029, 2015, URL: https://cds.cern.ch/record/2037702.

[53] ATLAS Collaboration, *Performance of pile-up mitigation techniques for jets in pp collisions at $\sqrt{s}$ = 8 TeV using the ATLAS detector*, Eur. Phys. J. C **76** (2016) 581, arXiv: 1510.03823 [hep-ex].

[54] ATLAS Collaboration, *Optimisation and performance studies of the ATLAS b-tagging algorithms for the 2017-18 LHC run*, ATL-PHYS-PUB-2017-013, 2017, URL: https://cds.cern.ch/record/2273281.

[55] ATLAS Collaboration, *Object based missing transverse momentum significance in the ATLAS detector*, ATLAS-CONF-2018-038, 2018, URL: https://cds.cern.ch/record/2630948.

[56] C. G. Lester and D. J. Summers, *Measuring masses of semi-invisibly decaying particles pair produced at hadron colliders*, Phys. Lett. B **463** (1999) 99, arXiv: hep-ph/9906349.

[57] A. Barr, C. Lester and P. Stephens, *A variable for measuring masses at hadron colliders when missing energy is expected; m(T2): the truth behind the glamour*, J. Phys. G **29** (2003) 2343, arXiv: hep-ph/0304226.

[58] ATLAS Collaboration, *Measurement of the top quark-pair production cross section with ATLAS in pp collisions at $\sqrt{s}$ = 7 TeV*, Eur. Phys. J. C **71** (2011) 1577, arXiv: 1012.1792 [hep-ex].

[59] ATLAS Collaboration, *Jet Calibration and Systematic Uncertainties for Jets Reconstructed in the ATLAS Detector at* $\sqrt{s}$ = 13 *TeV*, ATL-PHYS-PUB-2015-015, 2015, URL: https://cds.cern.ch/record/2037613.

[60] ATLAS Collaboration, *Jet energy scale measurements and their systematic uncertainties in proton-proton collisions at* $\sqrt{s}$ = 13 *TeV with the ATLAS detector*, Phys. Rev. D **96** (2017) 072002, arXiv: 1703.09665 [hep-ex].

[61] ATLAS Collaboration, *Expected performance of missing transverse momentum reconstruction for the ATLAS detector at* $\sqrt{s}$ = 13 *TeV*, ATL-PHYS-PUB-2015-023, 2015, URL: https://cds.cern.ch/record/2037700.

[62] ATLAS Collaboration, *Studies on top-quark Monte Carlo modelling for Top2016*, ATL-PHYS-PUB-2016-020, 2016, URL: https://cds.cern.ch/record/2216168.

[63] M. Baak et al., *HistFitter software framework for statistical data analysis*, Eur. Phys. J. C **75** (2015) 153, arXiv: 1410.1280 [hep-ex].

[64] A. L. Read, *Presentation of search results: The CL(s) technique*, J. Phys. G **28** (2002) 2693.